Geochemistry of cobalt-rich ferromanganese crusts from the Perth Abyssal Plain (E Indian Ocean)

Dominik Zawadzki[a,*], Łukasz Maciąg[a], Ryszard A. Kotliński[a], Gabriela A. Kozub-Budzyń[b], Adam Piestrzyński[b], Rafał Wróbel[c]

[a] Faculty of Geosciences, Natural Sciences Education and Research Centre, University of Szczecin, Mickiewicza 16a, 70-383 Szczecin, Poland
[b] AGH University of Science and Technology, Faculty of Geology, Geophysics and Environmental Protection, Department of Economic Geology, Mickiewicza 30, 30-059 Kraków, Poland
[c] Faculty of Chemical Technology and Engineering, West Pomeranian University of Technology Szczecin, Pułaskiego 10, 70-322 Szczecin, Poland

ARTICLE INFO

ABSTRACT

Geochemistry of cobalt-rich ferromanganese crusts from the as-yet-unexplored Dirck Hartog Ridge (DHR), a linear bathymetric feature of poorly understood origin, located in the centre of the Perth Abyssal Plain (PAP), is described for the first time, based on 3 samples analyzed with XRF, ICP-MS and EPMA. Mean bulk concentrations of Fe and Mn were 20.8 and 18.4 wt%, respectively; individual crust layers, however, proved chemically variable. The mean concentration of metals of the highest economic potential (Cu + Ni + Co) was 0.69 wt%. The mean total rare earth elements (REE) and yttrium (ΣREY) contents in the samples (1908 mg/kg) proved moderate. The crusts showed strong positive Ce anomalies, negative Y anomalies and a low Y_{SN}/Ho_{SN} ratio (mean 0.56). Observations on the texture and chemical composition of the crust samples studied allowed us to distinguish two major and two subtypes of representative colloform structures built of laminae. The Type I colloform structures showed the Mn/Fe ratio to range from 0.86 to 5.69, the ranges in Type II colloform structures being 0.49–2.47 (Subtype II-1) and 6.91–221.42 (Subtype II-2). The Subtype II-2 colloform structures were enriched in Ni (up to 7.31 wt%). The Co and Cu concentrations showed a high variability, 0.03–1.64 and 0.03–0.22 wt%, respectively. According to the current genetic models and discrimination diagrams, the crusts studied were classified as hydrogenetic, although individual laminae and groups of laminae could be regarded as diagenetic or hydrothermal.

1. Introduction

Marine ferromanganese (Fe-Mn) deposits (including polymetallic nodules and cobalt-rich crusts as the major types) have been, on account of their commercial potential, attracting wide interest for about 40 years (e.g. Shnyukov et al., 1979, Glasby et al., 1982; Halbach et al., 1988, Kotliński, 1999; Cronan, 2000; Hein and Koschinsky, 2014). Most of the economic research and exploration effort so far has been addressing polymetallic nodules and cobalt-rich ferromanganese crusts (e.g. Hein, 2000; Hein et al., 2015; Kotliński et al., 2015; Petersen et al., 2016).

Within the recent years, however, cobalt-rich Fe-Mn crusts have appeared in the focus as another promising source of important metals and minerals (Hein et al., 2013; Marino et al., 2017). Identification of the resource's potential calls for detailed geochemical studies which,

using e.g. the Mn-Fe and Ni-Co-Cu ratios, make it possible to, *inter alia*, infer the origin of the deposit's formation (hydrogenetic, diagenetic or hydrothermal) (Bonatti et al., 1972). In the recent years, the range of geochemical assays used for the purpose of identifying the deposit's origin has been augmented by discrimination diagrams based on rare earth elements (REE) and rare earth yttrium (REY) (Bau et al., 2014); in addition, the use of high field strength elements (HFSE) (Josso et al., 2017) has been proposed as well.

Most data on the distribution and resource potential of cobalt-rich Fe-Mn crusts have been collected from the Pacific (e.g. Hein et al., 2013, Hein and Koschinsky, 2014, Novikov et al., 2017), particularly from the Pacific Crust Zone (PPCZ). The PPCZ (or the Pacific Crust Zone, PCZ) is a seamount-rich region in the central and western equatorial Pacific, extending from the equator to 20°N (Hein et al., 2013). These seamounts are the biggest and the oldest in the global

ocean, their size and age acting in favour of the occurrence of thick crusts.

There is still not enough geochemical data available in the global data base and little is known about the abundance of the crusts in most areas of the ocean (Petersen et al., 2016). That is why studies like ours – not restricted to the Exclusive Economic Zones (EEZ) and International Seabed Authority (ISA) contracts generate an opportunity to complement knowledge on the geochemical nature and origin of Fe-Mn crusts. A comparison of data from different areas of the global ocean provides valuable insights into the variability of elemental concentrations in the Fe-Mn crusts.

Geochemical studies on the Pacific crusts revealed for instance that the chemical composition of crusts from the Shatsky Rise (SR, middle northern latitudes) was significantly different from that characterizing crusts from other regions of the Pacific (Hein et al., 2012). The SR crusts (collected mostly from depths larger than 3000 m) were high in Cu, Li and Th, and low in Co, Te and Tl, compared to the earlier studied crusts from the northwest-equatorial Pacific (Hein et al., 2000). Further, the SR crusts are strongly enriched in Th (152 ppm, with a mean of 56 ppm), compared to crusts from the equatorial Pacific. Detailed geochemical assays of individual layers of crusts from the Magellan Seamounts revealed Co, Ni, Cu and REE cations to be irregularly distributed in the crusts, which suggests that metal supplies to the deposits varied through time (Novikov et al., 2017).

As the interest in Fe-Mn crusts as a potential resource is growing, new locations are being explored (e.g. Konstantinova et al., 2017; Zhong et al., 2017), including those in the Indian Ocean. There, Fe-Mn crusts have been found in the Central Indian Ocean Basin (Jauhari and Pattan, 2000), on isolated seamounts such as the Afanasiy-Nikitin Seamount (Banakar et al., 2007) and on the Ninetyeast Ridge (Hein et al., 2016). Some of the crusts collected from the latter showed high concentrations of Co (0.91 wt%), Ni (0.43 wt%) and ΣREY (0.33 wt%) as well as the highest contents of Pt (1.5 ppm), Ru (52 ppb) and Rh (99 ppb) found so far in marine Fe-Mn deposits.

Recently, crust deposits have been located in the Perth Abyssal Plain (PAP; E Indian Ocean; Fig. 1). As there is a growing interest in Fe-Mn marine deposits world wide, comparative geochemical studies with crust discovered in different locations are especially important for understanding regional mechanisms underlying their formation and resource potential. The deposits described in this paper were sampled with the aim to perform detailed geochemical analyses, the results of which are reported in this paper. Those analyses provided grounds for making inferences, presented in the paper, as to the origin of the DHR crusts.

2. Area of study

The Perth Abyssal Plain (PAP) extends west of SW Australia; it was formed about 136 Ma when the seafloor between India, Australia and Antarctica was spreading and continents were drifting apart (Gibbons et al., 2012). It is flanked to the west by the Batavia Rise and Gulden Draak Knoll, associated with the northern Naturaliste Plateau and the western Bruce Rise, respectively (Whittaker et al., 2013), the eastern border being the continental rise of the Western Australian Shelf. To the north, PAP is bounded by the Zenith and the Cuvier Plateaux, the southern, more complex, boundary being built by the Broken Ridge and the Naturaliste Plateau separated by the Naturaliste Fracture Zone, Gonneville Triangle and the southernmost Diamantina Fracture Zone.

PAP is divided into the western and eastern parts by the Dirck Hartog Ridge (DHR), a linear feature more than 600 km long and trending NNE-SSW (~18°E), built by a group of irregular ridges rising to ~2000 m above the surrounding ocean floor. The wide (~50 km across) southern part of DHR deepens to a depth of 2800 m. The northern part, shaped like an elongated asymmetric mound, features shallower depths (~2200 m) and is about 30 km wide.

DHR is built of both intrusive and extrusive mafic igneous rocks

represented by alkali basalt in the northernmost and central parts as well as dolerite and gabbroic rocks in the south (Watson et al., 2016). Until recently, the DHR origin had been unclear. At present, it is interpreted to be an extinct spreading centre (Gibbons et al., 2012; Williams et al., 2013a) or a pseudofault (Mihut and Müller, 1998). The most recent research, however, indicates that the feature might be a volcano tectonic seamount chain associated with the Kerguelen plume (Watson et al., 2016).

The Eastern and Western PAP differ substantially in the bottom morphology. The Eastern PAP is characterized by a relatively smooth abyssal seafloor at a depth of 5000–5500 m, the Western PAP showing the presence of an ENE-WSW trending elongated ridge ~270 km in length. This ridge is orthogonal to DHS and surrounded by a number of variously oriented mounds (Watson et al., 2016).

The PAP sediment cover is relatively thin. As shown by the Deep Sea Drilling Program data from Sites 257 and 259, the basaltic basement is situated 262 m and 304 m below the seafloor (b.s.f.), respectively. Site 257 is located northeast of the Naturaliste Plateau, at a depth of 5278 m, whereas Site 259, 4712 m deep, is situated more to the west. The Site 257 sediment consists mainly of Cretaceous (Albian) to Quaternary brown detrital clay with a section of coccolith clay between 199 and 247 m b.s.f. Site 259 sediments are dated to the Aptian to Quaternary and represent green-gray clay, zeolitic clay, brown clay and oozes (Deep Sea Drilling Project, 1989).

PAP remains under the influence of two major water masses: the Western Australian Current (WAC), bringing cold water from high latitudes to the north, and the Leeuwin Current (LC), a south-flowing current carrying warm, low-salinity water from the tropics and high-salinity water from the subtropics along the western Australian coast (Cresswell and Golding, 1980; Richardson et al., 2005). LC is globally unique in being the only poleward-flowing eastern boundary current (comparable to the cold Benguela and Humboldt currents off the west coasts of Africa and South America, respectively). LC and its anticyclonic eddies affect the water column down to at least 1000 m and are low in nutrients and oxygen. Although this current system is observed most of the year, analysis of satellite-derived sea surface temperature images shows the strongest flows to occur between March and April (Cresswell and Peterson, 1993).

PAP, as a part of the Perth Basin, lies in the path of the Antarctic Bottom Water (AABW) and the Lower Circumpolar Deep Water (LCDW) flowing north into the Central Indian Basin through numerous deep sills in the Ninetyeast Ridge (Srinivasan et al., 2009). A southward return flow (between 2000 and 4000 m) of oxygen-poor and nutrient-enhanced water of the Indian Deep Water (IDW) overlays the northward flow of AABW and LCDW. As shown by current meter records at the southern opening of the Perth Basin between the Broken Ridge and the Naturaliste Plateau, the net northward transport is the strongest at the basin's western boundaries, the southward currents being at their strongest at the eastern boundaries. The transport in the middle of the basin is significantly weaker. The net northward transport below $\gamma^n > 28.1$ kg m^{-3} (≈ 3200 m) into the basin is between 4.4 and 5.8 Sv (LCDW 2.4 to 3.3 Sv and AABW 2.0 to 2.5 Sv) (Sloyan, 2006).

The water column salinity at 32°S varies between 35.5 PSU at the surface and 34.71 PSU at 4500 m. The sea surface temperatures in the northern and southern parts of PAP range from 18 °C in winter to 26 °C in summer, and from 15 °C in winter to 20 °C in summer, respectively. The temperature decreases with depth to 2.5 °C at 1500 m and 0.5 °C at 4500 m (Richardson et al., 2005; Sloyan, 2006; Cresswell and Domingues, 2009).

3. Materials and methods

3.1. Sample collection and processing

Fe-Mn crust samples from DHR-6 (sampling site #6 in the dredge log and in Fig. 1) were obtained in 2011, during cruise SS2011/06 of
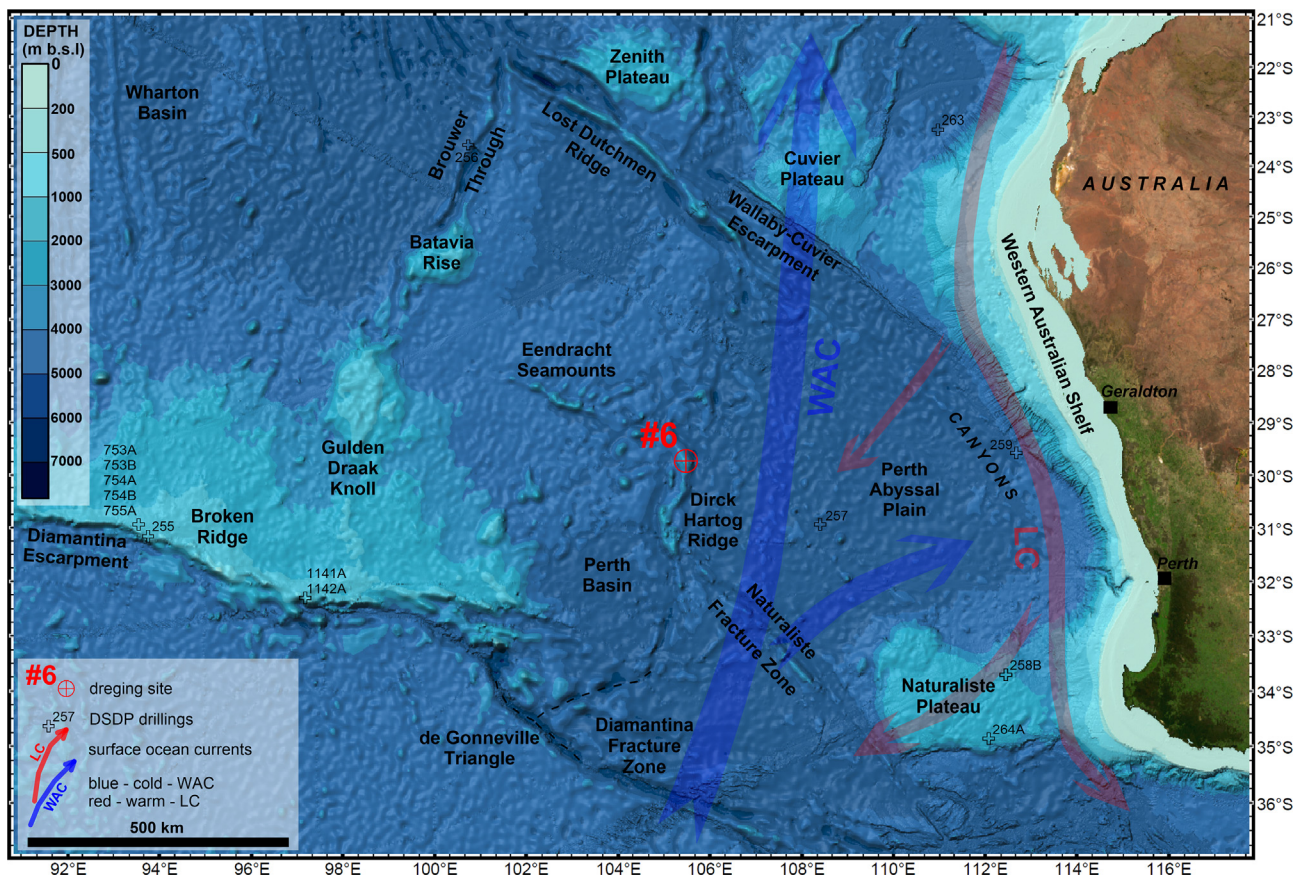
Fig. 1. Location of the sampling site on the Dirck Hartog Ridge visited during cruise SS2011/06. Bathymetry is based on GEBCO 2014 data. Names of the undersea features follow GEBCO Gazetteer (IHO-IOC, 2006).
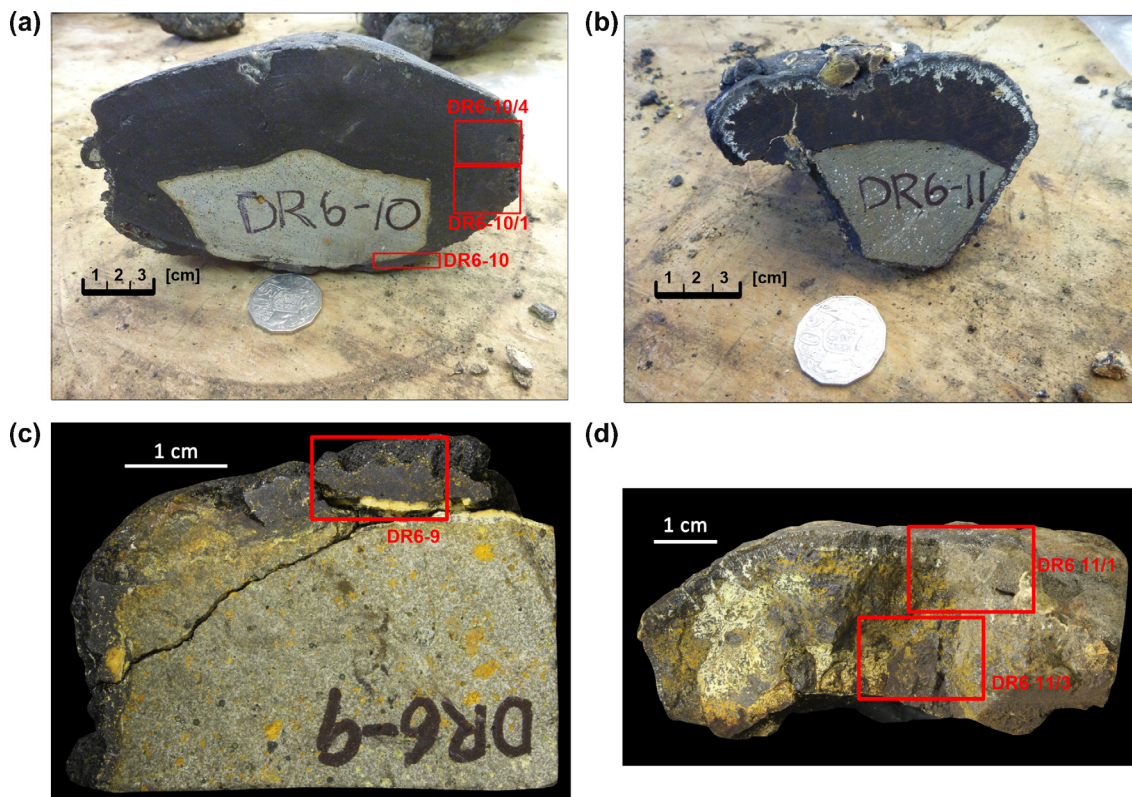

Fig. 2. Fe-Mn crusts from the Dirck Hartog Ridge, described in this paper. Red rectangles show crust fragments to be analyzed by XRF, ICP-MS and XRD.

Table 1

Chemical composition of bulk Fe-Mn crust samples from the Dirck Hartog Ridge, as determined by XRF and ICP-MS. ICP-MS: expanded uncertainty of the results: 25%, P = 95%, coverage factor k = 2. XRF precision accuracy (standard deviation) was determined after 24 experimental measurements (each measurement taking 8 min).

Element		DR6-9	DR6-10	DR6-10/1	DR6-10/4	DR6-11/1	DR6-11/3	Mean	Standard deviation*
Fe	wt%	20.2	20.7	25.3	24.3	11.4	23.2	20.8	0.07
Mn		15.7	20.9	20.7	23.1	12.9	17.2	18.4	0.06
Mn/Fe		0.8	1.0	0.8	0.9	1.1	0.7	0.9	
Si		8.05	5.17	2.55	2.28	9.21	5.36	5.44	0.08
Al		1.42	1.00	0.86	0.70	3.78	1.66	1.57	0.02
Mg		0.53	0.55	0.58	0.56	0.82	0.54	0.60	0.01
K		0.44	0.36	0.28	0.29	1.76	0.54	0.61	0.01
Ca		1.51	1.83	1.83	2.05	1.44	1.68	1.72	0.01
Na		0.40	0.36	0.29	0.36	1.07	0.44	0.49	0.06
P		0.14	0.17	0.21	0.22	0.10	0.16	0.17	0.001
Ti		0.66	0.81	1.57	1.33	0.94	1.43	1.12	0.01
S		0.14	0.17	0.17	0.19	0.10	0.15	0.15	0.002
Ag	mg/kg	1.9	4.1	1.2	3.1	1.4	3.2	2.5	
As		169	263	182	221	145	139	186	
Ba		1210	1830	1240	1660	1660	1490	1515	
Be		5.2	7.9	5.6	7.3	6.9	5.8	6.5	
Cd		3.2	4.6	3.2	3.7	2.8	2.9	3.4	
Co		3500	3390	3780	3350	2490	2330	3140	
Cr		9	63	9	19	6	10	19	
Cu		1270	1670	1180	1140	1050	1130	1240	
Li		7	9	6	5	41	52	20	
Mo		316	398	341	432	264	243	332	
Ni		2570	2550	2530	2440	2430	2780	2550	
Pb		932	1690	976	1140	915	883	1089	
Rb		9	10	9	7	22	27	14	
Sb		35	82	29	52	35	35	45	
Sr		1020	1340	1100	1290	981	873	1100	
Th		31	22	31	24	11	10	22	
Tl		108	129	123	121	76	80	106	
U		7.5	10.5	8.3	9.7	6.8	5.9	8.1	
V		507	652	530	639	506	478	552	
Zn		638	1040	593	724	689	667	725	
La		158	215	171	234	126	113	169	
Ce		1310	1300	1310	1410	1470	1350	1358	
Pr		32.9	46.1	35.0	49.0	24.4	21.5	34.8	
Nd		128	183	137	193	93	83	136	
Sm		27.1	38.3	29.3	40.6	18.1	16.7	28.3	
Eu		6.5	9.2	7	9.6	4.4	4	6.8	
Gd		29.5	40.7	31.6	43.5	20.3	19.0	30.8	
Tb		4.2	5.9	4.5	6.2	2.9	2.5	4.4	
Dy		24.5	34.4	26.3	36.3	17.3	14.8	25.6	
Y		79	97	82	105	53	48	77	
Ho		4.86	6.84	5.29	7.24	3.47	3.00	5.12	
Er		13.7	18.9	14.9	20.3	9.6	8.6	14.3	
Tm		2.0	2.6	2.1	2.8	1.3	1.1	2.0	
Yb		12.5	15.8	12.9	16.8	8.2	7.1	12.2	
Lu		1.90	2.39	1.96	2.55	1.25	1.08	1.9	
Sc		7	9	7	8	7	7	8	
ΣREY		1835	2017	1871	2177	1854	1694	1908	
ΣLREE		1662	1792	1689	1936	1736	1588	1734	
ΣHREE		172	225	182	241	117	106	174	
LREE/HREE		0.83	0.89	0.84	0.89	0.93	0.95	0.89	
Ce_{SN}/Ce_{SN}*		4.19	3.01	3.90	3.03	6.09	6.29	4.42	
Eu_{an}		1.07	1.09	1.07	1.07	1.07	1.04	1.07	
Y_{SN}/Ho_{SN}		0.60	0.52	0.57	0.53	0.56	0.59	0.56	

* XRF precision accuracy.

RV Southern Surveyor (operated by the Australian Marine National Facility), intended to collect new magnetic and swath bathymetry data and dredge rock samples from across PAP. The dredging was conducted along a 3-km long swath in the central part of the Dirck Hartog Ridge (coordinates of the dredging start and end: −29°41.828; 105°31.358 and −29°42.990; 105°29.871, respectively), covering the depth range of 2680–3345 m. The total weight of the 13 dredge samples obtained was about 30 kg. A number of samples showed the presence of a crust up to 45 mm thick (Fig. 2A–B). Prior to this study, only the substrate rocks were comprehensively described, the description showing the substrate rocks to be represented by amygdaloidal basalts with well-

developed Mn-oxide cemented tallus, altered basalts with microscopic vesicles filled with multiple fluid rims as well as strongly altered tallus clast. In addition, a small amount of ooze was collected in the dredge (Williams, 2011; Williams et al., 2013a,b; Whittaker et al., 2013; Watson et al., 2016).

In 2015, three DHR-6 samples (denoted DR6-9, DR6-10, DR6-11) were shipped to the laboratory of the Faculty of Geosciences, University of Szczecin, Poland for geochemical analyses. Representative sections of the crust and substrate rock were selected for the assays (Fig. 2C–D). Some sections were powdered by grinding in an agate mortar and the material was divided into three parts intended for energy dispersive X-
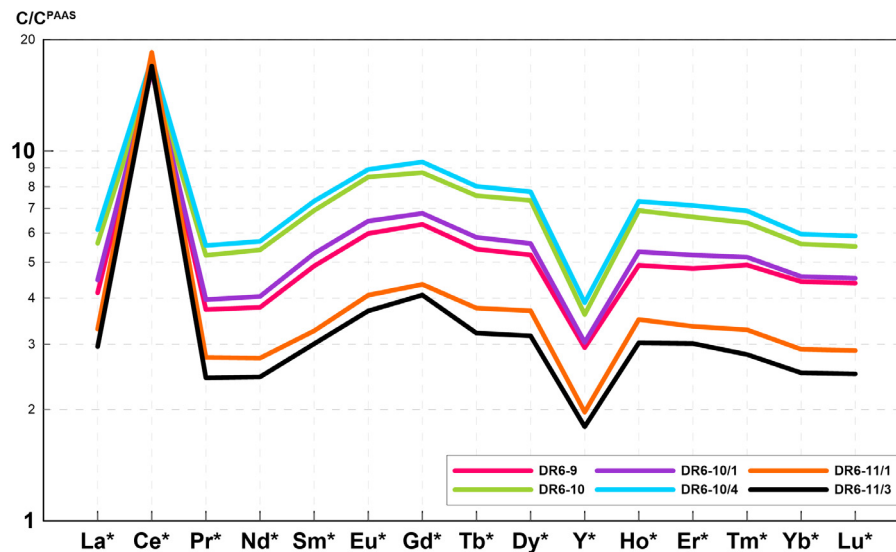
Fig 3. Post-Archean Australian Shale (PAAS)-normalized REE distribution in Fe-Mn crusts from the Dirck Hartog Ridge (PAAS according to Taylor and McLennan, 1985).

Table 2

Representative EPMA data (wt%) for Type I colloform structures (see Discussion); b.d.l., below detection limit. Since all As and Tl concentrations were below the EPMA detection limit, they are not shown.

No	K	Si	Al	Cl	Ba	Ca	Fe	Mn	Ti	P	Co	Ni	Cu	Zn	Sr	S	Pb	Na	Mg	Mn/Fe
1	0.21	3.67	0.95	0.75	0.42	1.90	26.39	22.70	2.55	0.44	0.38	0.26	0.14	0.17	b.d.l.	0.20	b.d.l.	0.62	0.40	0.86
2	0.07	2.78	0.78	0.42	0.32	2.30	20.49	21.41	1.11	0.35	0.67	0.31	0.15	b.d.l.	b.d.l.	0.23	0.38	0.49	1.00	1.05
3	0.39	0.52	1.59	0.29	0.15	1.57	6.32	36.26	0.38	0.13	0.43	3.03	0.37	b.d.l.	b.d.l.	0.25	b.d.l.	0.82	0.90	5.73
4	0.10	0.66	2.58	0.20	b.d.l.	1.44	6.02	35.84	0.20	0.12	0.23	3.20	0.75	0.15	b.d.l.	0.09	0.11	0.62	5.17	5.96
5	0.27	1.73	0.63	1.13	0.15	2.53	16.21	33.06	0.73	0.28	0.85	0.57	0.17	b.d.l.	b.d.l.	0.25	b.d.l.	0.40	0.94	2.04
6	0.23	3.49	0.93	0.87	0.50	1.81	26.17	22.50	2.24	0.45	0.32	0.19	0.12	0.14	b.d.l.	0.24	b.d.l.	0.99	0.82	0.86
7	0.36	1.40	0.58	0.39	0.20	3.17	15.22	33.82	0.88	0.27	1.44	0.65	0.13	0.11	0.13	0.23	0.23	0.84	1.25	2.22
8	0.19	2.71	0.64	0.41	0.16	2.89	18.67	21.20	2.67	1.38	1.04	0.23	0.12	0.12	b.d.l.	0.33	0.12	0.93	1.28	1.14
9	0.16	1.73	0.70	0.29	0.18	2.89	18.46	32.90	1.02	0.33	1.57	0.42	0.18	0.19	b.d.l.	0.14	0.14	0.53	0.94	1.78
10	0.28	1.62	0.38	0.85	0.30	2.74	18.37	30.04	1.19	0.25	1.10	0.29	b.d.l.	b.d.l.	b.d.l.	0.27	b.d.l.	0.52	0.90	1.64
11	0.25	1.42	0.35	0.77	0.24	2.68	15.64	30.92	1.11	0.21	1.09	0.43	0.12	0.42	b.d.l.	b.d.l.	b.d.l.	1.32	3.55	1.98
12	0.32	1.35	0.58	0.38	0.20	3.01	15.19	35.94	0.98	0.29	1.30	0.72	0.19	0.24	b.d.l.	b.d.l.	b.d.l.	1.57	3.93	2.37
13	0.08	1.77	0.68	0.97	0.16	2.94	14.69	32.92	0.80	0.24	1.29	0.60	0.12	b.d.l.	b.d.l.	0.34	b.d.l.	0.84	1.46	2.24
14	0.28	2.25	0.79	0.51	0.38	2.32	19.22	26.62	1.80	0.34	0.57	0.43	0.15	0.18	b.d.l.	0.25	0.13	0.59	0.82	1.39
15	0.29	1.89	0.69	1.09	0.16	2.76	16.96	32.56	0.69	0.30	1.00	0.57	0.16	0.11	b.d.l.	0.32	b.d.l.	1.02	1.04	1.92
16	0.36	1.75	0.72	0.59	0.12	3.11	15.17	34.39	0.69	0.26	0.91	0.79	0.20	0.15	b.d.l.	0.31	b.d.l.	1.19	1.20	2.27
17	0.34	1.64	0.69	0.58	0.15	3.12	13.95	34.18	0.65	0.24	0.68	0.81	0.19	0.15	b.d.l.	0.30	b.d.l.	1.00	1.13	2.45
18	0.25	2.58	0.68	0.83	0.24	2.50	22.40	27.07	1.83	0.42	0.41	0.44	0.13	b.d.l.	b.d.l.	0.34	b.d.l.	1.16	1.10	1.21
19	0.30	1.08	0.27	0.67	0.31	2.57	10.57	31.06	1.14	0.12	0.64	0.68	0.13	b.d.l.	b.d.l.	0.35	b.d.l.	0.84	0.91	2.94
20	0.28	1.48	0.28	1.04	0.19	2.29	17.08	25.78	0.93	0.24	0.75	0.36	0.06	b.d.l.	b.d.l.	0.30	b.d.l.	0.40	0.56	1.51
Mean	0.25	1.88	0.77	0.65	0.24	2.53	16.66	30.06	1.18	0.33	0.83	0.75	0.19	0.18	x	0.26	0.19	0.83	1.47	2.18
Standard deviation	0.09	0.81	0.50	0.28	0.10	0.50	5.13	4.97	0.67	0.26	0.38	0.81	0.15	0.08	x	0.07	0.10	0.31	1.21	1.34
Coeficient of variation	0.36	0.43	0.64	0.43	0.43	0.20	0.31	0.17	0.57	0.77	0.46	1.08	0.77	0.46	x	0.26	0.52	0.37	0.83	0.62
Detection limit	0.02	0.05	0.03	0.02	0.10	0.04	0.10	0.10	0.04	0.03	0.07	0.08	0.05	0.10	0.09	0.03	0.10	0.03	0.03	

ray Fluorescence Spectrometry (XRF), Inductively Coupled Plasma Mass Spectrometry (ICP-MS) and XRD assays (mineralogical analyses, to be described elsewhere; Maciąg et al., in prep.). Grain mounts from another group of sections were prepared for measurements in the electron probe microanalysis (EPMA). The sections were cut, mounted in epoxy resin and polished.

3.2. Geochemistry

XRF was carried out on powdered and press-pelleted samples to determine contents of 10 major oxides as well as V, Ni, Cu, Zn, Sr, Y, Zr, Nb, Mo, Ag, Ba, Nd and Pb. The analyses, following Brouwer (2010) were conducted using a PANalytical Epsilon 3 spectrometer at the Faculty of Chemical Technology and Engineering, West Pomeranian University of Technology, Szczecin, Poland.

Minor and trace element (including REY) contents were determined following Sindern (2017) after full acid digestion (HNO_3, HF, $HClO_4$ and *Aqua Regia*) by ICP-MS (ELAN DRC II, Perkin Elmer, USA) at the Central Chemical Laboratory of the Polish Geological Institute – National Research Institute (PGI-NRI), Warsaw, Poland. The ICP-MS data were normalized to Post Archean Australian Shale (PAAS) (Taylor and McLennan, 1985).

Back-scattered electron (BSE) images were obtained and compositional analyses were conducted at the Laboratory of Critical Elements, AGH University of Science and Technology, Cracow, Poland following Spilde and Berlin (2006) using a JEOL SuperProbe JXA-8230 electron probe microanalyzer (EPMA). EPMA was operated in the wavelength-dispersion mode at accelerating voltage of 15 kV, 20 nA probe current, 1 μm diameter focused beam for ferromanganese oxides, 3–5 μm diameter beam for apatite and aluminosilicates, counting times of 20 s at

Table 3
Representative EPMA data (wt%) for Subtype II-1 colloform structures (see Discussion); b.d.l., below detection limit. Since all As and Tl concentrations were below the EPMA detection limit, they are not shown.

No	K	Si	Al	Cl	Ba	Ca	Fe	Mn	Ti	P	Co	Ni	Cu	Zn	Sr	S	Pb	Na	Mg	Mn/Fe
1	0.10	3.41	1.28	0.35	0.22	1.75	21.37	20.97	0.97	0.34	0.39	0.35	0.19	0.12	b.d.l.	0.12	0.24	0.42	1.05	0.98
2	0.08	3.43	1.06	0.85	0.29	2.25	23.28	24.46	1.17	0.39	0.82	0.29	0.15	b.d.l.	b.d.l.	0.25	0.38	0.38	1.01	1.05
3	0.08	3.58	1.14	0.94	0.29	2.28	23.81	23.88	1.20	0.38	0.81	0.26	0.16	b.d.l.	b.d.l.	0.23	0.35	0.44	0.87	1.00
4	0.58	5.16	2.36	0.37	0.14	1.92	14.74	25.32	0.57	0.28	0.41	0.80	0.17	0.15	b.d.l.	0.17	b.d.l.	0.60	1.33	1.72
5	0.44	2.57	1.81	0.30	0.22	1.93	13.12	32.35	0.51	0.26	0.89	1.51	0.45	0.13	b.d.l.	0.18	b.d.l.	0.70	2.21	2.47
6	0.26	2.38	1.31	0.36	0.19	2.51	15.70	31.31	0.64	0.37	0.38	0.79	0.18	b.d.l.	b.d.l.	0.21	b.d.l.	0.38	1.14	1.99
7	0.19	5.43	2.45	0.71	0.40	2.10	26.49	16.53	3.68	0.47	0.35	0.19	0.11	0.17	b.d.l.	b.d.l.	0.13	0.39	0.72	0.62
8	0.27	2.66	0.96	0.84	0.27	2.23	21.37	27.33	0.85	0.39	0.32	0.43	0.18	b.d.l.	b.d.l.	0.19	b.d.l.	0.34	0.73	1.28
9	0.30	1.98	0.41	0.95	0.32	2.53	17.35	26.15	0.99	0.33	0.84	0.30	0.09	0.11	b.d.l.	0.16	0.12	0.63	0.52	1.51
10	0.21	4.72	0.73	0.64	0.36	1.60	30.02	17.47	1.28	0.38	0.15	0.20	0.09	b.d.l.	b.d.l.	0.21	b.d.l.	0.54	0.56	0.58
11	0.21	4.82	0.96	0.56	0.54	1.47	33.25	16.37	1.24	0.41	0.21	0.18	0.12	0.11	b.d.l.	0.25	0.16	0.80	0.92	0.49
12	0.50	4.79	1.13	0.51	0.27	1.37	21.29	17.91	0.89	0.20	0.35	0.19	b.d.l.	0.21	b.d.l.	0.20	0.35	0.72	0.57	0.84
13	0.16	1.89	0.36	0.53	0.18	2.25	16.14	21.61	1.15	0.26	0.45	0.19	0.10	0.12	0.10	0.18	0.35	0.64	0.61	1.34
14	0.18	2.49	0.49	0.49	0.28	2.17	19.35	20.46	1.29	0.31	0.36	0.22	b.d.l.	b.d.l.	b.d.l.	0.10	b.d.l.	0.58	0.52	1.06
15	0.09	4.90	1.46	0.83	0.65	1.61	29.05	15.32	4.78	0.39	0.28	0.15	0.07	0.17	0.10	0.17	0.31	0.04	0.21	0.76
Mean	0.24	3.61	1.19	0.62	0.31	2.00	21.76	22.50	1.41	0.34	0.47	0.40	0.16	0.14	x	0.19	0.27	0.51	0.86	1.18
Standard deviation	0.15	1.21	0.61	0.22	0.13	0.36	5.78	5.19	1.15	0.07	0.24	0.36	0.09	0.03	x	0.04	0.10	0.19	0.46	0.57
Coeficient of variation	0.61	0.33	0.51	0.35	0.43	0.18	0.27	0.23	0.81	0.20	0.51	0.88	0.58	0.23	x	0.22	0.37	0.37	0.53	0.45
Detection limit	0.02	0.05	0.03	0.02	0.10	0.04	0.10	0.10	0.04	0.03	0.07	0.08	0.05	0.10	0.09	0.03	0.10	0.03	0.03	

Table 4
Representative EPMA data (wt%) for Subtype II-2 colloform structures (see Discussion); b.d.l., below detection limit. Since all As and Tl concentrations were below the EPMA detection limit, they are not shown.

No	K	Si	Al	Cl	Ba	Ca	Fe	Mn	Ti	P	Co	Ni	Cu	Zn	Sr	S	Pb	Na	Mg	As	Mn/Fe
1	1.78	b.d.l.	0.20	b.d.l.	0.14	0.27	0.38	47.43	0.29	b.d.l.	0.95	1.98	0.19	0.14	b.d.l.	b.d.l.	b.d.l.	1.32	3.52	b.d.l.	123.75
2	1.04	4.35	2.36	0.37	0.30	1.65	4.83	34.76	1.03	0.16	0.32	1.90	0.41	0.24	b.d.l.	0.14	b.d.l.	0.87	2.58	0.26	7.20
3	0.73	1.85	0.99	0.65	0.44	2.35	5.40	37.31	1.46	0.26	0.31	1.52	0.30	0.16	b.d.l.	0.13	b.d.l.	0.85	1.44	0.11	6.91
4	1.44	b.d.l.	0.57	0.07	0.16	0.99	0.30	46.73	0.05	0.05	b.d.l.	1.56	1.07	0.16	b.d.l.	0.13	b.d.l.	0.85	1.44	0.11	156.95
5	0.75	1.93	1.20	0.51	0.44	2.95	5.77	40.60	1.21	0.18	0.35	1.74	0.33	0.19	b.d.l.	b.d.l.	b.d.l.	0.19	2.84	b.d.l.	7.04
6	0.11	b.d.l.	1.06	0.06	b.d.l.	2.09	0.20	41.42	b.d.l.	b.d.l.	0.60	6.75	0.37	0.22	b.d.l.	b.d.l.	b.d.l.	2.46	2.14	b.d.l.	211.42
7	1.37	b.d.l.	0.62	0.10	0.29	1.00	0.43	47.91	0.08	0.06	b.d.l.	1.34	0.95	0.39	b.d.l.	b.d.l.	b.d.l.	0.50	4.54	b.d.l.	112.46
8	0.13	b.d.l.	1.06	0.03	b.d.l.	2.05	0.21	40.56	b.d.l.	b.d.l.	1.64	6.36	0.28	0.15	b.d.l.	b.d.l.	b.d.l.	2.46	2.09	b.d.l.	189.05
9	0.07	b.d.l.	3.12	0.03	b.d.l.	1.03	0.42	35.61	b.d.l.	b.d.l.	0.42	7.31	0.33	b.d.l.	b.d.l.	b.d.l.	b.d.l.	1.45	4.45	b.d.l.	83.89
10	0.35	0.57	3.45	0.17	b.d.l.	1.15	1.39	39.01	0.21	0.07	b.d.l.	3.44	1.22	0.50	b.d.l.	0.06	b.d.l.	0.66	5.65	0.13	28.05
11	0.55	0.53	3.17	0.23	0.18	1.33	1.90	40.25	0.25	0.12	0.18	3.53	0.92	0.57	b.d.l.	0.09	b.d.l.	0.87	5.10	0.07	21.18
12	0.35	0.65	2.85	0.12	b.d.l.	1.21	1.16	40.00	0.18	0.08	0.21	3.61	1.00	0.13	b.d.l.	0.29	0.11	1.19	1.02	b.d.l.	34.58
13	0.77	0.32	1.58	0.11	0.31	1.18	1.33	45.46	0.39	0.05	0.17	3.04	0.68	0.17	0.10	0.17	0.31	0.21	0.76	b.d.l.	34.12
14	1.03	0.06	1.19	0.13	b.d.l.	1.05	0.34	46.69	0.12	0.06	b.d.l.	2.70	1.02	0.43	b.d.l.	0.04	b.d.l.	0.83	5.91	b.d.l.	139.33
15	1.56	0.11	0.30	0.03	0.49	0.53	0.75	47.80	0.14	b.d.l.	0.63	2.14	0.41	0.20	0.12	0.07	b.d.l.	1.19	3.42	b.d.l.	63.91
Mean	0.80	1.15	1.58	0.19	0.31	1.39	1.65	42.10	0.45	0.11	0.53	3.26	0.63	0.26	x	0.12	0.21	1.06	3.13	0.14	81.32
Standard deviation	0.54	1.30	1.07	0.19	0.12	0.68	1.91	4.40	0.47	0.07	0.42	1.92	0.30	0.14	x	0.07	0.10	0.65	1.64	0.06	67.39
Coeficient of variation	0.67	1.13	0.68	0.99	0.40	0.49	1.16	0.10	1.04	0.61	0.79	0.59	0.55	0.54	x	0.57	0.48	0.61	0.52	0.48	0.83
Detection Limit	0.02	0.05	0.03	0.02	0.10	0.04	0.10	0.10	0.04	0.03	0.07	0.08	0.05	0.10	0.09	0.03	0.10	0.03	0.03	0.04	

the peak and 10 s against both positive (+) and negative (−) backgrounds. The data were corrected with the ZAF procedure using the JEOL electron microprobe software.

Wavelength-Dispersive X-ray Spectroscopy (WDS) X-ray maps of ferromanganese oxides were developed using a 15 kV accelerating voltage, 20 nA beam current, 15 ms dwell time, 0.5 μm step size and a focused beam.

To determine the growth rate of the DHR crusts, Manheim & Lane-Bostwick "Cobalt chronometer" was applied (Manheim and Lane-Bostwick, 1988). The calculated growth rates need to be considered as maximum ones, as the method is not sensitive to hiatuses. The growth rate (R) was calculated for the bulk samples from $R = 6.8 \times 10^{-1}/(Co^n)^{1.67}$ [mm/My], where: $Co^n = Co \times 50/Fe + Mn$.

3.3. Data processing

The data were processed by calculating basic statistical parameters and Pearson correlation coefficients (StatSoft Statistica v. 8) to develop a correlation matrix of elemental contents and concentrations. The tertiary diagram was plotted using the Grapher v. 10 (Golden Software Inc.).

4. Results

4.1. Physical description

The analyzed crusts were from 2 to 45 mm thick and showed a large-scale botryoidal texture with fine-scale microbotryoidal texture at the very surface, with only small (to 4–5 mm) protrusions. The crusts were massive, laminated and somewhat more porous in the surface part, contacting tightly and uniformly with the substrate. As shown by the chemical data and results of the XRD analysis, the main mineral phases are represented by Fe-Mn oxyhydroxides (vernadite, asbolane, feroxyhyte-ferrihydryte). The crust surfaces showed small fractures and cavities, filled – as confirmed by subsequent analyses – with zeolites, clay minerals and phosphates. Phosphate minerals were represented mainly by amorphous (Ca)-hydroxy(fluoro)apatite and collophane, mixed with clays (nontronite, saponite, celadonite, glauconite, Fe-chlorites) and Fe-Mn oxyhydroxides, especially at the crust-substrate border (the yellowish layer in Fig. 2C). (Maciąg et al., in prep.). The same material was also observed within the uppermost part of the substrate rock. Inside, the crusts were mostly black or dark grayish, and some showed thin layers and mottling of yellow-orange minerals
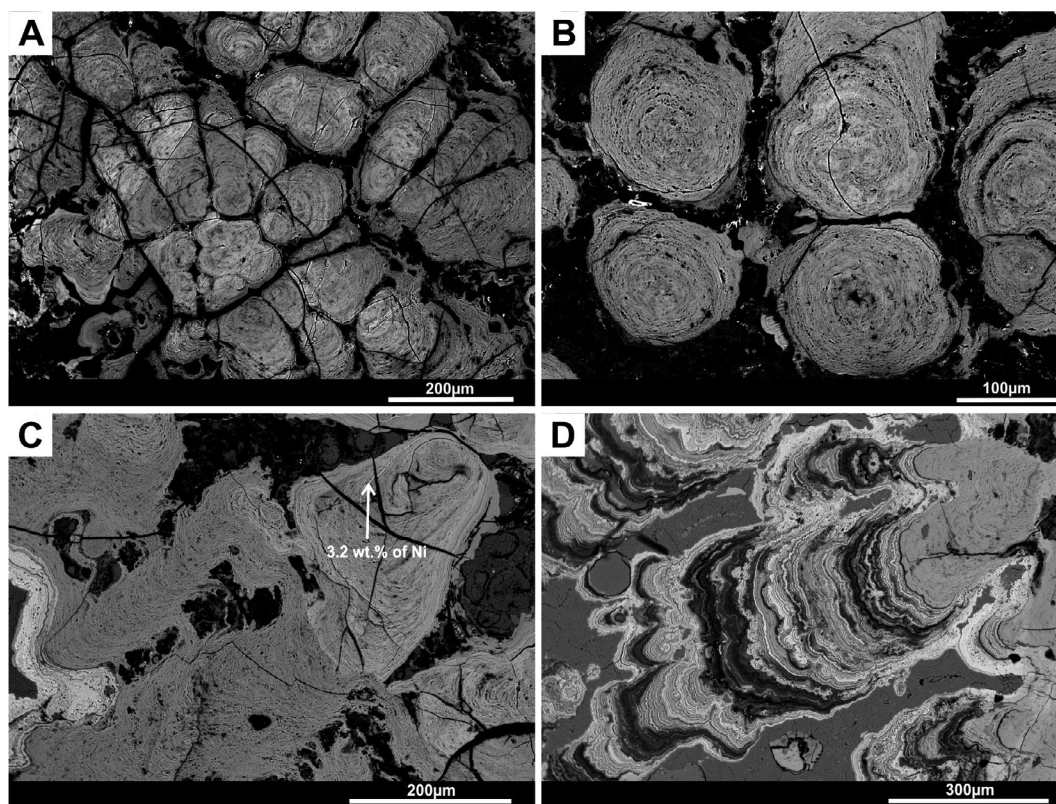
Fig. 4. Cobalt-rich ferromanganese crusts in BSE images; A, B, Type I colloforms (sample DR6-10); C, bright laminae of Mn oxides, enriched in Ni in Type I colloform, with outermost layers of Type II-2 colloform (light gray on the left hand side of the photo; sample DR6-11); D, Type I colloform overgrown by Type II-2 colloform (sample DR6-11).

(Fig. 2B).

4.2. XRF and ICP-MS

As shown by the XRF and ICP-MS-determined concentrations of major, minor and trace elements in each Fe-Mn crust sample (Table 1), Fe and Mn varied from 11.4 to 25.3 wt% and from 12.9 to 23.1 wt%, respectively. The average Mn/Fe ratio was 0.9. The combined content of Cu + Ni + Co ranged from 0.62 to 0.76 wt%, with an average of 0.69 wt%. Since the crusts studied were slightly phosphatized, the phosphorus concentration was low (< 0.22 wt%). The Zn + Pb content ranged from 1550 to 2730 mg/kg, averaging 1814 mg/kg.

The mean Si, Al and K concentrations were 5.44, 1.57 and 0.61 wt%, respectively; on the other hand, the crusts showed low mean concentration of Na (0.49 wt%) and Mg (0.60 wt%). The Ca concentration varied from 1.44 to 2.05 wt%, averaging 1.72 wt%. The Ba content ranged from 1210 to 1830 mg/kg (averaging 1515 mg/kg). The Ag concentrations were unusually high for Fe-Mn crust, as they ranged from 1.2 to 4.1 mg/kg, with an average of 2.5 mg/kg.

The total REY (ΣREY) contents ranged from 1694 to 2177 mg/kg (averaging 1908 mg/kg). The metal most abundant amongst REY was Ce, occurring with a mean content of 1358 mg/kg. The samples studied showed strong positive Ce anomalies ($Ce_{SN}/Ce_{SN}^* = 3.01$–6.28) (where $Ce_{SN}^* = 0.5La_{SN} + 0.5\,Pr_{SN}$) (Bau et al., 2014), clearly seen on the REE distribution spider diagrams (Fig. 3). The samples exhibited also slightly positive Eu anomalies ($Eu_{an} = 1.04$–1.09) and a Gd anomaly which is common in crust (Hein et al., 2012) as well as some depletion in LREE relative to HREE (0.83–0.95) [where $LREE_{SN}/HREE_{SN} = (La_{SN} + 2Pr_{SN} + Nd_{SN})/(Er_{SN} + Tm_{SN} + Yb_{SN} + Lu_{SN})$ (Dubinin and Sval'nov, 2000)]. The samples analyzed displayed negative Y anomalies.

4.3. EPMA

The EPMA results showed individual types of laminae to be highly variable in their chemical composition. The Mn and Fe concentrations varied from 15.32 to 36.26 wt% and from 6.02 to 33.25 wt%, respectively. The Mn/Fe ratio ranged from 0.86 to as high as 221.42. The Ni concentrations ranged from 0.19 to 3.20 wt%. The Co and Cu concentrations were highly variable, the ranges being as wide as 0.03–1.64 and 0.03–1.22 wt%, respectively. The Mg concentrations were highly variable as well (0.40–5.91 wt%). The Si, Al and K concentrations changed from below the detection limit to 5.43, 0.20–3.45 and 0.07–1.78 wt%, respectively (Tables 2–4).

Observations on the texture and chemical composition of the crust samples studied allowed us to distinguish two major and two subtypes of representative colloform structures built of laminae. The Type I colloform structures are characterized by high porosity and poorly visible borders between the laminae (Fig. 4A–C), whereas the Type II colloform structures are more condensed, the laminae being sharply delineated (Fig. 4D).

4.3.1. Type I colloform structures

The Type I colloform structures are highly porous, variability of their chemical composition being moderate; it was only Ni, Cu, P and Mg contents that were substantially more variable. The laminae are concentric and uniform (Fig. 4A–C). The Mn and Fe concentrations range within 21.20–36.26 and 6.02–26.36 wt%, respectively. The Mn/Fe ratio range is 0.86–5.69. The Ni, Co and Cu concentration ranges are 0.19–0.81, 0.23–1.57 and 0.06–0.75 wt%, respectively. Occasionally, Type I colloforms feature thin (< 1 μm) microlaminae of a higher reflexivity (Fig. 4C), enriched in Ni (up to 3.2 wt%) and Mg (up to 5.17 wt%; Table 2).
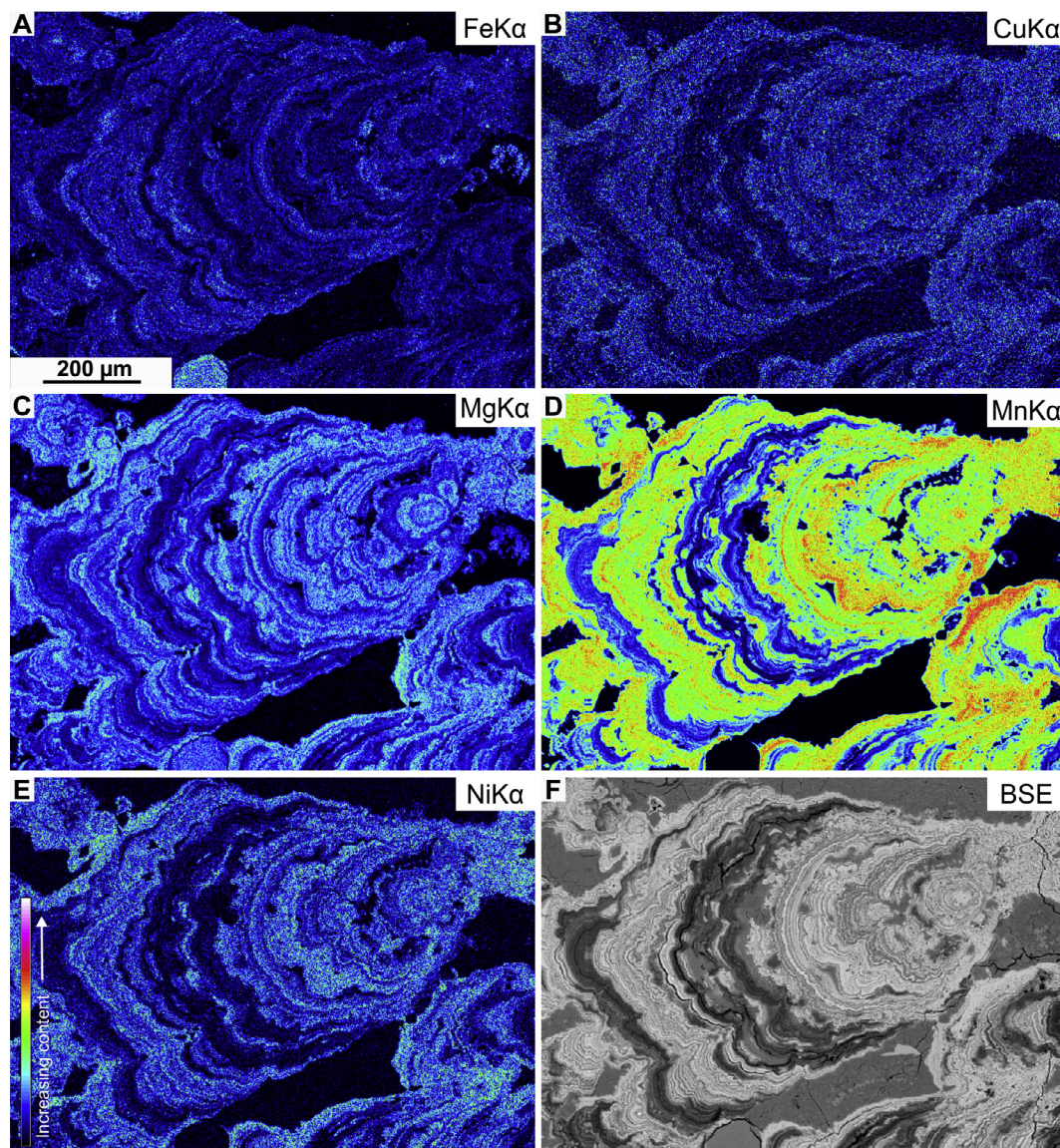
Fig. 5. X-ray maps and BSE images of Type II colloform; Sample DR6-11/1_A1. The dark layers poor in the elements discussed are aluminosilicates.

4.3.2. Type II colloform structures

The Type II colloform structures are characterized by a denser and non-uniform texture, compared to Type I; however, the differences in the contents of chemical components between the laminae are not so distinctive as in Type I (Figs. 4D, 5). Based on the chemical composition of the laminae, the Type II colloforms can be further subdivided into subtypes. In Subtype II-1, the Mn/Fe ratio spans a range of 0.49–2.47, with Mn and Fe contents ranging within 15.32–32.35 and 13.12–33.25 wt%, respectively. The contents of Ni, Co and Cu are as high as < 1.51, < 0.89 and < 0.45 wt%, respectively (Table 3). Some Fe-dominated laminae show high Ti contents (Table 3, Nos. 7, 15). The Mn/Fe ratio in the Subtype II-2 is much higher (6.91–221.42) than in the Type I and Subtype II-1, with higher concentrations of Ni (up to 7.31 wt%) and Mg (up to 5.65 wt%) and low Fe concentrations averaging 1.6 wt% (Table 4). The differences between the two colloform subtypes are also reflected in the contents of alkali metals, phosphorus and sulphur: the Subtype II-2 colloforms contain less Si, Ca and P and more Mg, compared to Subtype II-1 (Tables 3 and 4).

4.4. Correlations

As shown by the correlation coefficient matrix (Table 5), Fe is

negatively correlated with Mn, Ni, Cu, Zn, Al, Ca, K, Na, Mg, positive correlation being revealed with P, Si and Ti. Mn is positively correlated with Ni, Cu, Zn, Ca, K, Na, Mg, and negatively with P, Si and Ti. Cu, Ni and Zn are positively correlated with each other and also with Al, K, Na and Mg, whereas they correlate negatively with Cl, P, Pb, S and Si. Co shows strong positive correlations with Ca and S and to some extent with Cl and Na, a weak correlation being revealed with Mn and negative correlations with Al, As, Cu, Fe, Mg and Zn. Si is positively correlated with P and negatively with Ca, K, N, Na and Mg. Al shows negative correlations with Ba, Ca, Cl, P, Pb and S and positive correlations with, As, Tl and Mg.

5. Discussion

5.1. Elements concentration comparisons with other regions

According to their macroscopic features and geochemical data (Table 1), the samples examined can be classified as representing typical cobalt-rich Fe-Mn crusts. The DHR crusts studied showed higher Fe concentrations, compared to those found in the deposits from the Ninetyeast Ridge and the Pacific Prime Crust Zone (Fig. 6). Compared to crusts from the Atlantic and other parts of the Indian Ocean, the Mn

Table 5

Matrix of correlation coefficients for EPMA-derived contents and concentrations of selected major and trace elements; all the significant (p < 0.05) correlations are marked red; n = 127.

	Si	Al	Cl	Ba	Ca	Fe	Mn	Ti	P	Co	Ni	Cu	Zn	K	Sr	S	Pb	Tl	Na	Mg	As
Al	0.17																				
Cl	-0.06	-0.39																			
Ba	0.02	-0.26	0.40																		
Ca	-0.32	-0.36	0.70	0.15																	
Fe	0.59	-0.25	-0.02	0.18	-0.38																
Mn	-0.71	0.07	0.04	-0.13	0.42	-0.95															
Ti	0.10	-0.07	0.07	0.39	-0.23	0.46	-0.53														
P	0.25	-0.25	0.40	0.31	0.32	0.46	-0.44	0.32													
Co	-0.22	-0.40	0.42	0.00	0.75	-0.23	0.29	-0.18	0.21												
Ni	-0.53	0.53	-0.45	-0.37	-0.17	-0.69	0.62	-0.34	-0.60	-0.11											
Cu	-0.46	0.58	-0.45	-0.32	-0.27	-0.61	0.58	-0.33	-0.50	-0.38	0.68										
Zn	-0.37	0.57	-0.36	-0.17	-0.27	-0.53	0.50	-0.21	-0.45	-0.39	0.59	0.85									
K	-0.26	0.09	-0.29	-0.10	-0.22	-0.58	0.58	-0.29	-0.48	-0.22	0.32	0.50	0.51								
Sr	0.04	0.02	0.20	0.40	0.05	0.01	0.04	0.05	0.15	-0.06	-0.02	-0.06	-0.06	-0.08							
S	-0.21	-0.46	0.79	0.23	0.91	-0.15	0.22	-0.14	0.38	0.68	-0.39	-0.41	-0.37	-0.30	0.12						
Pb	0.18	-0.24	0.41	0.48	0.34	0.17	-0.19	0.03	0.56	0.21	-0.39	-0.38	-0.31	-0.38	0.26	0.37					
Tl	-0.01	0.27	-0.32	-0.05	-0.15	-0.18	0.12	-0.05	-0.23	-0.15	0.27	0.25	0.16	0.14	0.20	-0.23	-0.17				
Na	-0.54	-0.02	0.03	-0.09	0.31	-0.71	0.72	-0.37	-0.38	0.29	0.64	0.30	0.24	0.40	0.10	0.17	-0.15	0.14			
Mg	-0.44	0.66	-0.50	-0.36	-0.29	-0.68	0.63	-0.33	-0.59	-0.29	0.83	0.89	0.80	0.56	-0.04	-0.44	-0.42	0.25	0.42		
As	0.04	0.38	-0.22	0.19	-0.18	-0.06	0.00	0.19	-0.09	-0.27	0.13	0.28	0.35	0.22	-0.08	-0.21	-0.15	0.21	-0.08	0.29	
H$_2$O$^-$*	-0.14	-0.02	0.01	-0.27	0.16	-0.48	0.32	-0.47	-0.27	0.11	0.25	0.12	0.06	0.18	-0.26	0.00	-0.06	-0.01	0.21	0.18	-0.24

* Calculated as the rest from the EMPA analysis.
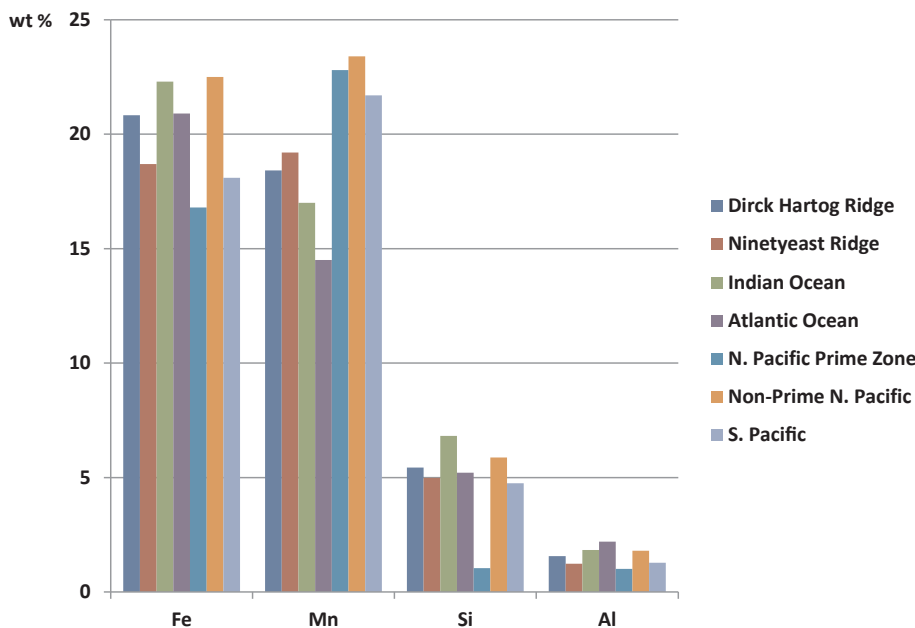
Fig. 6. Mean concentrations of major elements in the Dirck Hartog Ridge crusts against mean values in crusts from other areas of the World's Ocean; the Ninetyeast Ridge, Indian Ocean data after Hein et al. (2016); the means for the Indian and Atlantic Oceans, North Pacific Prime Zone, Non-Prime North Pacific and South Pacific data after Hein et al. (2013).

concentrations were higher as well. On the other hand, the contents of Co + Cu + Ni were generally lower. The mean contents of Co, Cu and Ni (3140, 1240 and 2550 mg/kg, respectively) were similar to those in crusts from other parts of the Indian Ocean (3291, 1105, 2563 mg/kg, respectively; Hein and Koschinsky, 2014), but lower than those in the PCZ (6662, 976 and 4209 mg/kg, respectively; Hein and Koschinsky, 2014), (Fig. 7). The DHR crust Co and Ni contents were substantially lower than reported for the Southern Pacific (6167 mg/kg and 4643 mg/kg, respectively; Hein and Koschinsky, 2014). Compared to the crusts from the Ninetyeast Ridge, west of the present area of study, the DHR crusts are slightly depleted in Co and slightly enriched in Cu (3872 mg/kg and 1024 mg/kg, respectively; Hein et al., 2016).

The mean Si, Al and K (6.82, 1.83 and 0.63 wt%, respectively) concentrations in the samples studied proved similar to those found in crusts from other areas of the Indian Ocean (Hein and Koschinsky, 2014). The mean Ba contents were also similar to those reported from other areas of the Indian Ocean (1515 mg/kg for DHR vs 1533 mg/kg as the mean for Indian Ocean) (Hein et al., 2013). The DHR samples were depleted in ΣREY (1908 mg/kg) relative to the crusts from other areas (Hein et al., 2013, 2015, 2016); it was only in the Southern Pacific that the crusts contained slightly less ΣREY (Hein et al., 2013), compared to the values found in this study (Fig. 7).

The mean concentrations of Co and Ni found in the DHR crusts (0.31 wt% and 0.25%, respectively) are typical of globally recognized "younger" crusts (Halbach and Manheim, 1984). The positive Mn correlation with Ni, Cu and Zn suggests domination of precipitation of typical Fe-Mn oxyhydroxide colloids which acquire trace metals by surface sorption processes; however, this is not confirmed by the Ba and
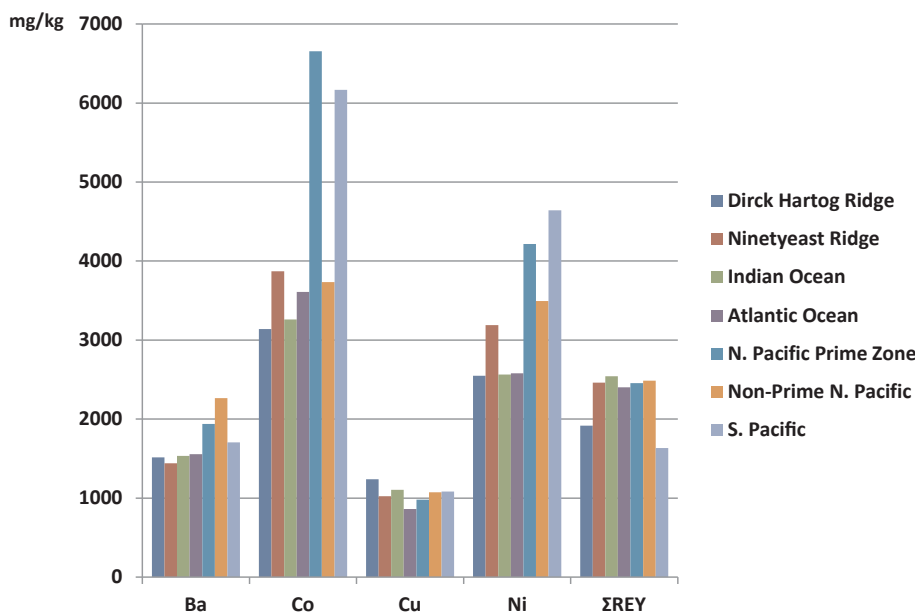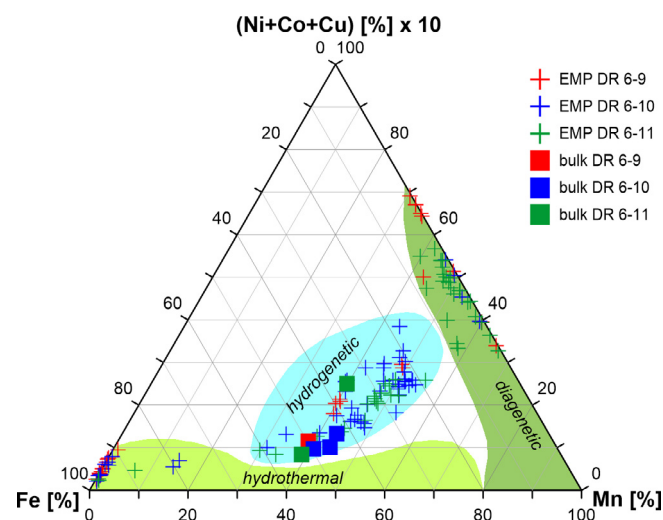
Fig. 8. A traditional ternary discrimination diagram (Bonatti et al., 1972) of the samples studied. All the bulk samples are placed in the hydrogenetic field, but different individual layers are located in hydrogenetic, diagenetic or hydrothermal fields.

Tl correlations (Hein et al., 2013). In the samples studied, Fe correlated positively with phosphorus and aluminosilicate detritus elements, typical of the Fe-dominated laminae. A higher correlation of Co with S in the Fe-Mn laminae, as seen in the DHR crusts, suggests some additional cobalt acquisition from hydrothermal sources (Zeng et al., 2010). It may be connected also with the complex redissolution, reorganization and secondary enrichment processes due to alteration or phosphatisation (Koschinsky et al., 1997). Fe and Mn are found mainly in vernadite, feroxyhyte-ferrihydrite and asbolane (Maciąg et al., in prep.) which adsorb heavy manganophilic metals (Co, Ni, Zn) and have large chemically active surfaces, affecting higher metal concentration in individual crust layers (Novikov et al., 2014). Along with Ba, Sr, P, Cl and S, Fe should be considered as residual biogenic input (Hein and Koschinsky, 2014). The Ti enrichment in Fe-dominated laminae suggests hydrogenetic growth of several laminae on highly oxidized Fe-rich mineral surfaces (Koschinsky and Hein, 2003); however, the impact of some oxic diagenetic factors should be considered as substantial for the formation of some laminae. The contents of Ni and Cu increase in the

Fe-Mn laminae with Mn/Fe ratio < 5 (Type I and Subtype II-2 colloform structures) and decrease with Mn/Fe ratio > 5 (Type I Nos. 3, 4; Subtype II-2) (Halbach et al., 1981). High Ag concentrations may be explained as the evidence of the hydrothermal input (Hein et al., 2005). Other possibility is the diagenetic Ag incorporation within clay minerals (Bolton et al., 1986). However, further studies are required to explain increased Ag concentrations in the DHR Fe-Mn crusts.

The high phosphorus content and the presence of layers of Fe-Mn oxyhydroxides may be also indicative of changes in hydrodynamic conditions, inflows of oxygenated deep water and upwellings (Marino et al., 2017). Therefore, major phosphatized colloforms may be formed under stable conditions supporting slower diagenetic growth.

5.2. Origin of the crusts studied

As mentioned in the Introduction, the conventional distinction between hydrogenetic, diagenetic and hydrothermal Fe-Mn deposits is based on a ternary Mn vs Fe vs (Cu + Ni + Co) × 10 diagram (Bonatti et al., 1972). However, this approach is not sufficient to distinguish between hydrothermal and diagenetic precipitates. This is illustrated by Fig. 8; although all the bulk samples in our study could be classified as hydrogenetic, different individual layers should be considered as hydrogenetic, diagenetic or hydrothermal.

The uncertain distinction between the hydrothermal and diagenetic origins of the Fe-Mn layers in the samples examined led us to follow the innovative approach of Bau et al. (2014) involving the use of discrimination diagrams based on ΣREE and ΣREY as the components with behaviours coherent with the marine environment. The two resultant discrimination diagrams show relationships between the $Ce_{SN}/Ce_{SN}*$ ratio vs the Nd concentration and the $Ce_{SN}/Ce_{SN}*$ ratio vs the Y_{SN}/Ho_{SN} ratio, respectively. The two bivariate diagrams clearly show the samples analyzed to represent hydrogenetic Fe-Mn crusts, with a relatively high Ce anomaly, a low Y_{SN}/Ho_{SN} ratio and a high ΣREY (Fig. 9). The only two exceptions are samples DR6-11/1 and DR6-11/3 with lower Nd concentrations (93.3 and 83.0 mg/kg, respectively), more typical of hydrogenetic Fe-Mn nodules. However, the remaining parameters are typical of hydrogenetic crusts. The large positive Ce anomalies in the samples (averaging 4.42) can be related to a slow growth rate of the crust (Kuhn et al., 1998). The bulk crust growth rate normally ranges between 1 and 15 mm/My (most frequently 4–6 mm/My) for hydrogenetic crusts (Nagender Nath et al., 1997). The crust growth rate for the bulk DHR samples varies from 2 to 5 mm/My, with mean 3.93
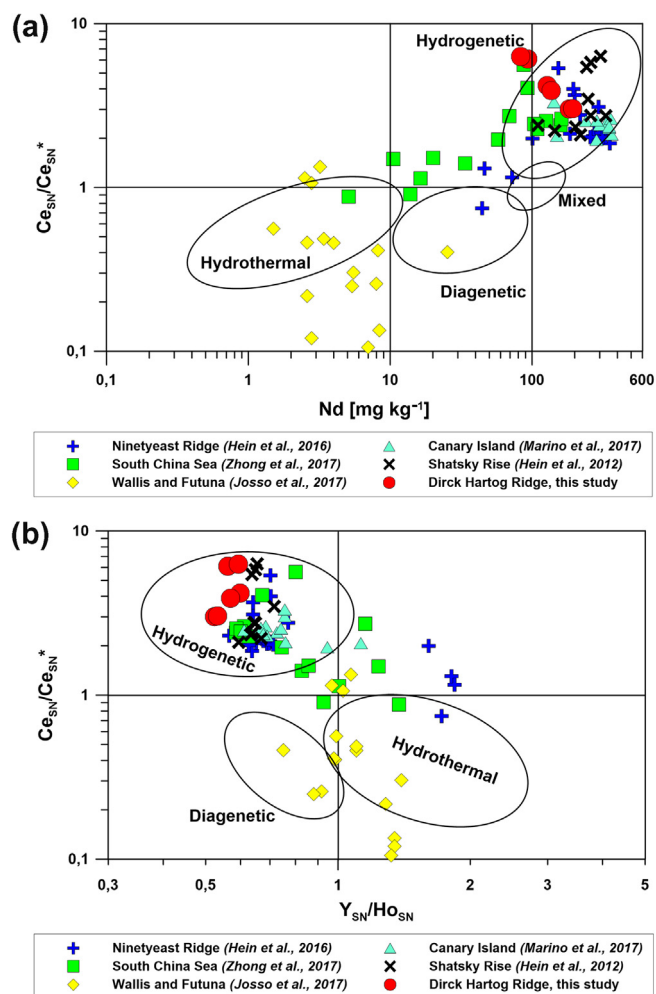
Fig. 9. Comparison of discrimination diagrams of marine Fe-Mn deposits from several locations: Ninetyeast Ridge, Indian Ocean (Hein et al., 2016); South China Sea (Zhong et al., 2017); Wallis and Futuna, southwest Pacific Ocean (Josso et al., 2017); Canary Island Seamount Province, northeastern tropical Atlantic (Marino et al., 2017); Shatsky Rise, northwest Pacific (Hein et al., 2012); Dirck Hartog Ridge, this study (solid red circles). A, Ce_{SN}/Ce_{SN}^* ratio vs Nd concentration; B, Ce_{SN}/Ce_{SN}^* ratio vs Y_{SN}/Ho_{SN} ratio (Bau et al., 2014). SN = PAAS-normalized REE. (For interpretation of the references to colour in this figure legend, the reader is referred to the web version of this article.)

(~ 4) mm/My, which is typical of the hydrogenetic origin. As the DHR crusts studied were up to 45 mm thick, their age is inferred to be at least 14.4 Ma.

A variety of marine Fe-Mn deposits from several locations having different oceanographic and tectonic settings are shown in Fig. 9. Although most (notably those from the Shatsky Rise, Canary Island Seamount Province) can be regarded as purely hydrogenetic, samples from the Wallis and Futuna are typical hydrothermal deposits with low ΣREE (14–39 ppm), variable positive and negative Ce anomalies as well as the Nd content below 10 mg/kg⁻ in most samples. The large variability of the South China Sea (SCS) data are due to some samples being from the north-eastern and some from the north-western parts of SCS (NESCS and NWSCS, respectively). The NESCS nodules exhibit no Ce anomalies and low Nd concentrations (Fig. 9a); in addition, the samples show negative Y and Ce anomalies (Fig. 9b), which allows to regard the material as diagenetic. However, two of the samples are located in the hydrothermal field. On the other hand, most NWSCS samples are grouped in the purely hydrogenetic crust field with large positive Ce and negative Y anomalies, as well as a high Nd content. As mentioned by Zhong et al. (2017), positive Ce anomalies as well as high Ti and Co

contents reflect water-mass dissolved metal composition and terrigenous input. The DHR samples showed negative Y anomalies (Fig. 3), typical of hydrogenetic crusts. Nevertheless, a geochemistry-based comparison between oceanic hydrogenetic and hydrothermal crusts and metalliferous hydrothermal sediments from different areas may be in some cases insufficient and fail to identify hydrothermal input in ferromanganese crusts of mixed composition (Baturin and Dubinchuk, 2011). Four of the Ninetyeast Ridge samples lie outside the fields shown in Fig. 9, because the crusts are phosphatized, which the discrimination diagram could not account for. The remaining crusts, non-phosphatized, are typically hydrogenetic (Hein et al., 2016).

6. Summary

Cobalt-rich ferromanganese (Fe-Mn) crusts from the Dirck Hartog Ridge (DHR), located in the centre of the Perth Abyssal Plain (E Indian Ocean) were analyzed and described for the first time.

The average combined concentration of metals of the highest commercial potential (Cu + Ni + Co) was 0.69 wt%, which is similar to the mean for the Indian Ocean crust and lower than in the crusts from the Pacific Crust Zone (1.18 wt%). Compared to crusts from other areas, the samples studied were depleted in rare earth elements and yttrium (mean ΣREY = 1908 mg/kg), the Southern Pacific crusts only containing less ΣREY.

The crusts studied showed strong positive Ce anomalies, negative Y anomalies and low Y_{SN}/Ho_{SN} ratios (mean 0.56). Based on the existing genetic models and discrimination diagrams, the crusts studied were classified as hydrogenetic, although individual layers showed also features indicating diagenetic and hydrothermal origin.

The study provides new data for inclusion into the global database of chemical composition of oceanic crusts. However, as the number of samples analyzed in this study was low, unequivocal conclusions as to the geochemical patterns observed and crust origin require additional samples from the area.

References

Banakar, V.K., Hein, J.R., Rajani, R.P., Chodankar, A.R., 2007. Platinum group elements and gold in ferromanganese crusts from Afanasiy-Nikitin Seamount, equatorial Indian Ocean. J. Earth Syst. Sci. 116, 3–13.

Bau, M., Schmidt, K., Koschinsky, A., Hein, J., Kuhn, T., Usui, A., 2014. Discriminating between different genetic types of marine ferro-manganese crusts and nodules based on rare earth elements and yttrium. Chem. Geol. 381, 1–9.

Baturin, G.N., Dubinchuk, V.T., 2011. Mineralogy and chemistry of ferromanganese crusts from the Atlantic Ocean. Geochem. Int. 49 (6), 578–593. https://doi.org/10.1134/S0016702911060024.

Bolton, B.R., Ostwald, J., Monzier, M., 1986. Precious metals in ferromanganese crusts from the south-west Pacific. Nature 320, 518–520. https://doi.org/10.1038/320518a0.

Bonatti, E., Kraemer, T., Rydell, H., 1972. Classification and genesis of submarine iron–manganese deposits. In: Horn D.R. (Ed.), Papers from a Conference on Ferromanganese Deposits on the Ocean Floor, Natl. Sci. Found., 149–166.

Brouwer, P., 2010. Theory of XRF: Getting Acquainted with the Principles. PANalytical, Almela, Netherlands.

Cresswell, G.R., Golding, T.J., 1980. Observations of a south-flowing current in the southeastern Indian Ocean. Deep-Sea Res. 27A, 449–466. https://doi.org/10.1016/

0198-0149(80)90055-2.

Cresswell, G.R., Peterson, J.L., 1993. The Leeuwin Current south of Western Australia. Aust. J. Mar. Freshw. Res. 44, 285–303.

Cresswell, G.R., Domingues, C.M., 2009. The Leeuwin Current south of Western Australia. J. R. Soc. Western Australia 92, 83–100. http://www.rswa.org.au/publications/Journal/92(2)/ROY%20SOC%2092.2%2LEEUWIN%2083-100.pdf.

Cronan, D.S. (Ed.), 2000. Handbook of Marine Minerals Deposits. CRC Press, Boca Raton, pp. 347–368.

Deep Sea Drilling Project, 1989. Archive of Core and Site/Hole Data and Photographs from the Deep Sea Drilling Project (DSDP). https://doi.org/10.7289/V54M92G2.

Dubinin, A.V., Sval'nov, V.N., 2000. Geochemistry of rare earth elements in micro and macronodules from the pacific bioproductive zone. Lithology and Mineral Resources, Vol. 35, No. 1, pp. 19–31. Translated from Litologiya i Poleznye Iskopaemye, No. 1, 2000, pp. 25–39.

Gibbons, A., Barckhausen, U., Van Den Bogaard, P., Hoernle, K., Werner, R., Whittaker, J.M., Müller, R.D., 2012. Constraining the Jurassic extent of Greater India: tectonic evolution of the Australian margin. Geochem., Geophy., Geosyst. 13. https://doi.org/10.1029/2011GC003919.

Glasby, G., Stoffers, P., Sioulas, A., Thijssen, T., Friedrich, G., 1982. Manganese nodule formation in the Pacific Ocean: a general theory. Geo-Mar. Lett. 2 (1–2), 47–53.

Halbach, P., Scherhag, C., Hebisch, U., Marchig, V., 1981. Geochemical and mineralogical control of different genetic types of deep-sea nodules from the Pacific Ocean. Min. Deposita 16, 59–84.

Halbach, P., Manheim, F.T., 1984. Potential of cobalt and other metals in ferromanganese crusts on seamounts of the Central Pacific Basin. Mar. Min. 4 (4), 319–336.

Halbach, P., Friedrich, G., von Stackelberg, U., 1988. The manganese nodule belt of the Pacific Ocean. Geological Environment, Nodule Formation, and Mining Aspects. Ferdinand Enke Verlag, Stuttgart.

Hein, J.R., 2000. Cobalt-rich ferromanganese crusts: global distribution, composition, origin and research activities. In: Polymetallic Massive Sulphides and Cobalt-Rich Ferromanganese Crusts: Status and Prospects, International Seabed Authority: Kingston.

Hein, J.R., Koschinsky, A., Bau, M., Manheim, F.T., Kang, J.-K., Roberts, L., 2000. Cobalt-rich ferromanganese crusts in the Pacific. In: Cronan, D.S. (Ed.), Handbook of Marine Mineral Deposits. CRC Press, Boca Raton, Fla, pp. 239–279.

Hein, J.R., Koschinsky, A., McIntyre, B.R., 2005. Mercury and silver-rich ferromanganese oxides, southern california borderland: deposits model and environmental implications. Economic Geol. 100 (6), 1151–1168.

Hein, J.R., Conrad, T.A., Frank, M., Christl, M., Sager, W.W., 2012. Copper-nickel-rich, amalgamated ferromanganese crust-nodule deposits from Shatsky Rise, NW Pacific. Geochem. Geosyst. 13 (10).

Hein, J.R., Mizell, K., Koschinsky, A., Conrad, T.A., 2013. Deep-ocean mineral deposits as a source of critical metals for high- and green-technology applications: comparison with land-based resources. Ore Geol. Rev. 51, 1–14. https://doi.org/10.1016/j.oregeorev.2012.12.001.

Hein, J.R., Koschinsky, A., 2014. Deep-ocean ferromanganese crusts and nodules. In: In: Scott, S. (Ed.), The Treatise on Geochemistry v. 12. Elsevier, pp. 273–291.

Hein, J., Spinardi, F., Okamoto, N., Mizell, K., Thorburn, D., Tawake, A., 2015. Critical metals in manganese nodules from the Cook Islands EEZ, abundances and distributions. Ore Geol. Rev. 68, 97–116. https://doi.org/10.1016/j.oregeorev.2014.12.011.

Hein, J.R., Conrad, T., Mizell, K., Banakar, V.K., Frey, F.A., Sager, W.W., 2016. Controls on ferromanganese crust composition and reconnaissance resource potential, Ninetyeast Ridge, Indian Ocean. Deep-Sea Res. I 110, 1–19. https://doi.org/10.1016/j.dsr.2015.11.006.

IHO-IOC, 2006. GEBCO Gazetteer of Undersea Feature Names, 2006 version.

Josso, P., Pelleter, E., Pourret, O., Fouquet, Y., Etoubleau, J., Cheron, S., Bollinger, C., 2017. A new discrimination scheme for oceanic ferromanganese deposits using high field strength and rare earth elements. Ore Geol. Rev. 87, 3–15. https://doi.org/10.1016/j.oregeorev.2016.09.003.

Jauhari, P., Pattan, J.N., 2000. Ferromanganese nodules from the Central Indian Ocean Basin. In: Cronan, D. (Ed.), Handbook of Marine Mineral Deposits. CRC Press, London, pp. 171–197.

Konstantinova, N., Cherkashov, G., Hein, J.R., Mirão, J., Dias, P., Madureira, P., Kuznetsov, V., Maksimov, F., 2017. Composition and characteristics of the ferromanganese crusts from the western Arctic Ocean. Ore Geol. Rev. 87, 88–99. https://doi.org/10.1016/j.oregeorev.2016.09.011.

Koschinsky, A., Stascheit, A., Bau, M., Halbach, P., 1997. Effects of phosphatization on the geochemical and mineralogical composition of marine ferromanganese crusts. Geochim. Cosmochim. Acta 61, 4079–4094.

Koschinsky, A., Hein, J.R., 2003. Uptake of elements from seawater by ferromanganese crusts: solid phase association and seawater speciation. Mar. Geol. 198, 331–351. https://doi.org/10.1016/S0025-3227(03)00122-1.

Kotliński, R., 1999. Metallogenesis of the World's ocean against the background of oceanic crust evolution. Special Papers, Polish Geological Institute, No. 4.

Kotliński, R., Maciąg, Ł., Zawadzki, D., 2015. Potential and recent problems of the possible polymetallic sources in the oceanic deposits. Geol. Miner. Resour. World Ocean 40 (2), 65–80.

Kuhn, T., Bau, M., Blum, N., Halbach, P., 1998. Origin of negative Ce anomalies in mixed hydrothermal-hydrogenetic Fe–Mn crusts from the Central Indian Ridge. Earth Planet. Sci. Lett. 163, 207–220.

Maciąg, Ł., Zawadzki, D., Kotliński, R.A., Kozub-Budzyń, G., Piestrzyński, A., Wróbel, R., 2018. Mineralogy of Cobalt-rich ferromanganese crusts from the Perth Abyssal Plain (E Indian Ocean) (in prep.).

Manheim, F.T., Lane-Bostwick, C.M., 1988. Cobalt in ferromanganese crusts as a monitor of hydrothermal discharge on the Pacific sea floor. Nature 335, 59–62.

Marino, E., González, F.J., Somoza, L., Lunar, R., Ortega, L., Vázquez, J.T., Reyes, J., Bellido, E., 2017. Strategic and rare elements in Cretaceous-Cenozoic cobalt-rich ferromanganese crusts from seamounts in the Canary Island Seamount Province (northeastern tropical Atlantic). Ore Geol. Rev. 87, 41–61. https://doi.org/10.1016/j.oregeorev.2016.10.005.

Mihut, D., Müller, R.D., 1998. Volcanic margin formation and Mesozoic rift propagators in the Cuvier Abyssal Plain off Western Australia. J. Geophys. Res.: Solid Earth 103 (B11), 135–149. https://doi.org/10.1029/97JB02672. 27.

Nagender Nath, B., Plüger, W.L., Roelandts, I., 1997. Geochemical constraints on the hydrothermal origin of ferromanganese encrustations from the Rodriguez Triple Junction, Indian Ocean. Geological Society, London, Special Publications 119, 199–211.

Novikov, G.V., Yashina, S.V., Melnikov, M.E., Vikentev, I.V., Bogdanova, O.Yu., 2014. Nature of co-bearing ferromanganese crusts of the magellan seamounts (Pacific Ocean): Communication 2. Ion exchange properties of ore minerals. Lithol. Miner. Resour. 49 (2), 138–164.

Novikov, G.V., Melnikov, M.E., Bogdanova, O.Yu, Drozdova, A.N., Lobus, N.V., 2017. Mineralogy and geochemistry of co-bearing manganese crusts from the govorov and volcanologist guyots of the magellan seamounts (Pacific Ocean). Oceanology 57 (5), 716–722 ISSN 0001–4370.

Petersen, S., Krätschell, A., Augustin, N., Jamieson, J., Hein, J.H., Hannington, M.D., 2016. News from the seabed – Geological characteristics and resource potential of deep-sea mineral resources. Mar. Policy 70, 175–187. https://doi.org/10.1016/j.marpol.2016.03.012.

Richardson, L., Mathews, E, Heap, A., 2005. Geomorphology and Sedimentology of the South Western Planning Area of Australia. Review and synthesis of relevant literature in support of Regional Marine Planning. Geoscience Australia. Canberra, Australia.

Shnyukov, E.F., Beloded, R.M., Tsemko, V.P., 1979. Mineral Resources of the Oceans. Naukova Dumka, Kiev, pp. 1–259.

Sindern, S., 2017. Analysis of Rare Earth Elements in Rock and Mineral Samples by ICP-MS and LA-ICP-MS. Phys. Sci. Rev. 2 (2). https://doi.org/10.1515/psr-2016-0066.

Sloyan, B.M., 2006. Antarctic bottom and lower circumpolar deep water circulation in the eastern Indian Ocean. J. Geophys. Res. 111, C02006. https://doi.org/10.1029/2005JC003011.

Spilde, M.N., Berlin, J., 2006. JEOL JXA-8200 SuperProbe. University of New Mexico, Department of Earth and Planetary Science and Institute of Meteoritics, pp. 1–29.

Srinivasan, A., Garraffo, Z., Iskandarani, M., 2009. Abyssal circulation in the Indian Ocean from a 1/12° resolution global hindcast. Deep-Sea Res. I 56, 1907–1926.

Taylor, S.R., McLennan, S.M., 1985. The Continental Crust: Its Composition and Evolution. Blackwell Scientific Publication, Carlton, pp. 1–312.

Watson, S.J., Whittaker, J.M., Halpin, J.A., Williams, S.E., Milan, L.A., Daczko, N.R., Wyman, D.A., 2016. Tectonic drivers and the influence of the Kerguelen plume on seafloor spreading during formation of the Early Indian Ocean. Gondwana Res. https://doi.org/10.1016/j.gr.2016.03.009.

Whittaker, J.M., Halpin, J.A., Williams, S.E., Hall, L.S., Gardner, R., Kobler, M.E., Daczko, N.R., Müller, R.D., 2013. Tectonic Evolution and Continental Fragmentation of the Southern West Australian Margin. West Australian Basins Symposium Perth, WA, 18–21 August 2013.

Williams, S.E., 2011. The Perth Abyssal Plain: Understanding Eastern Gondwana Break-up, RV Southern Surveyor Voyage SS2011_v06 Scientific Highlights, CSIRO, http://www.marine.csiro.au/nationalfacility/voyagedocs/2011/index.htm.

Williams, S.E., Whittaker, J.M., Granot, R., Müller, D.R., 2013a. Early India-Australia spreading history revealed by newly detected Mesozoic magnetic anomalies in the Perth Abyssal Plain. J. Geophys. Res.: Solid Earth 118 (7), 3275–3284. https://doi.org/10.1002/jgrb.50239.

Williams, S.E., Whittaker, J.M., Müller, D.R., 2013b. Newly-recognised Continental Fragments Rifted from the West Australian Margin. West Australian Basins Symposium. Perth, WA, 18–21 August 2013.

Zeng, Z., Chen, D., Yin, X., Hiao, Y.W., Xiao, H., Wang, M., 2010. Elemental and isotopic compositions of the hydrothermal sulfide on the East Pacific Rise near 13°N. Sci. China Earth Sci. 253–266. https://doi.org/10.1007/s11430-010-0013-3.

Zhong, Y., Chen, Z., González, F.J., Hein, J.R., Zheng, X., Li, G., Luo, Y., Mo, A., Tian, Y., Wang, S., 2017. Composition and genesis of ferromanganese deposits from the northern South China Sea. J. Asian Earth Sci. 138, 110–128. https://doi.org/10.1016/j.jseaes.2017.02.015.